



A simplified photogrammetry procedure in oil-film interferometry for accurate skin-friction measurement over arbitrary geometries

Igal Gluzman¹ · Patrick Gray¹ · Kevin Mejia² · Thomas C. Corke¹ · Flint O. Thomas¹

Received: 20 March 2022 / Accepted: 10 June 2022 / Published online: 15 July 2022
© The Author(s), under exclusive licence to Springer-Verlag GmbH Germany, part of Springer Nature 2022

Abstract

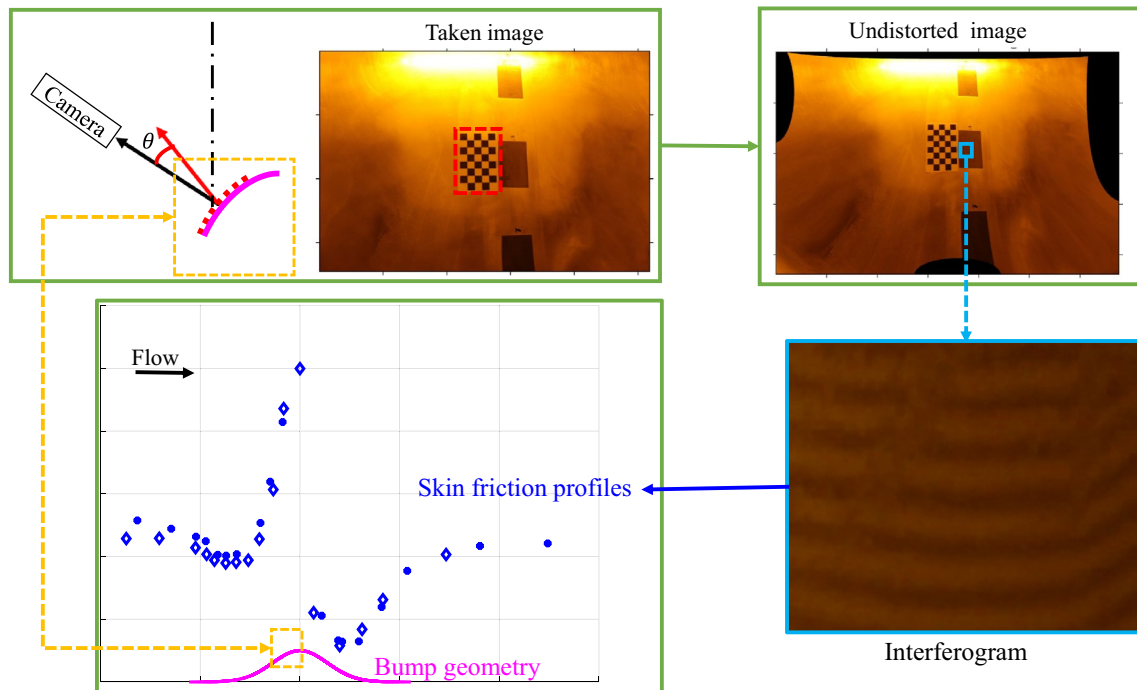
An accurate and straightforward skin-friction measurement procedure over a three-dimensional (3D) bump geometry is proposed. The procedure employs oil-film interferometry (OFI) measurements coupled with photogrammetry techniques. Photogrammetry is vital for accurate quantitative skin friction measurements over curved surfaces and at different oil flow imaging settings. However, it requires information on surface geometry obtained from multiple reference points on the surface and placing the camera in the exact location and orientation before and after the wind-tunnel run, which complicates the application of OFI. A new simplified method reported here is based on camera calibration algorithms and a flexible small checkerboard. The proposed procedure removes the elaborate steps typically performed in photogrammetry while retaining the same measurement accuracy. In particular, *it allows obtaining OFI data without a priori knowledge of model geometry and only taking images after experiments at arbitrary undocumented camera locations*. The simplified method was first validated with the Clauser method over a flat surface in a canonical turbulent boundary layer. Then the method was applied to obtain the skin-friction distribution for turbulent flow over 3D Gaussian bump geometry, which exhibits smooth body flow separation. The obtained high-quality benchmark data over the bump geometry are aimed to serve as validation data for numerical simulations for the challenging task of predicting flow separation.

✉ Igal Gluzman
igluzman@nd.edu; igal.gluzman@gmail.com

¹ Institute for Flow Physics and Control, Aerospace and Mechanical Engineering Department, University of Notre Dame, Notre Dame, IN 46556, USA

² The Boeing Company, Seattle, WA 98108, USA

Graphical abstract



1 Introduction

Skin-friction measurements are essential for characterizing and studying the topology of flow fields. In aerodynamic studies, it is crucial for assessing viscous drag over flight vehicles and airfoil models (Mateer et al. 1996), determining the position of separation (Wadcock et al. 1999; Liu 2019), location of laminar-turbulent boundary layer (TBL) transition (Von Karman 1934; Dong et al. 2018), and because of its high sensitivity to the velocity profile above the wall (Womack et al. 2019), it is often used in simulation validations (Naughton et al. 2006).

Out of available wall shear stress measurement techniques, image-based oil-film interferometry (OFI) (Tanner and Blows 1976) is one of the most accurate (typical uncertainty of within 3 %) and reliable methods of mean skin-friction measurements (Naughton and Sheplak 2002; Driver 2003). The technique has been applied in different setups, geometries, and flow regimes, such as large wind tunnels (Driver 2003), turbulent boundary layers (Bourassa and Thomas 2009; Naughton and Hind 2013), three-dimensional boundary layers (Ruedi et al. 2003), low-speed flows over 3D surfaces (Naughton et al. 2006; Lunte and Schüle 2020), and 3D supersonic flow (Baldwin et al. 2019). Being versatile, relatively inexpensive, having a short setup time,

and accurate, OFI is recommended to be used as the standard for mean skin-friction measurements and to be a part of all validation experiments conducted in wall-bounded flows where computations perform poorly (Nagib et al. 2006).

In this technique, an oil is applied to the model before experiments. The flow-induced shear thins the oil during the experiment. This localized thickness of the thin oil layer is used as an input to the thin-oil-film equation to obtain the local skin friction (Squire 1961). The method accuracy relies on the determination of the oil viscosity as a function of temperature during the experiment and the ability to accurately evaluate the end state of oil thickness (after the experimental run) from the acquired interferogram images by assessing the spacing between the fringes in the resulting fringe pattern (Monson et al. 1993). The only significant errors in the OFI method are those that occur from measuring the oil viscosity and computation of fringe spacing from interferogram images (Monson et al. 1993; Rezaeiravesh et al. 2018).

Recent advances in controlled temperature wind-tunnel experiments and the processing of the images using advanced digital acquisition and processing, such as the use of photogrammetry (Liu et al. 2000, 2012) and improved analysis routines (Naughton et al. 2003; Naughton and Hind 2013), allow one to maintain an OFI accuracy of 2–3% (and even less than 1% if great care is

taken) in a wide range of imaging setups and complex test model geometries (Naughton and Liu 2007). In particular, photogrammetry in OFI is used to determine the relationship between three-dimensional object coordinates and corresponding two-dimensional image coordinates to accurately obtain the oil thickness, for which precise camera incidence angle to each point in the interferogram on the model surface is necessary.

The two-step photogrammetry approach discussed in Naughton and Liu (2007) is used to eliminate all of the errors in determining the incidence angle due to surface curvature and also due to close camera proximity to the model surface. In addition, their approach allows for relaxing the requirement of precise measurement of camera location during testing and makes the computation of the incidence angle and model surface location for each point in the image plane straightforward. On models with significant surface curvature, such as the NASA bump model (Naughton et al. 2006), the combined effects of camera proximity and model curvature made photogrammetry critical to calculating accurate skin-friction values.

However, there is some complexity in applying photogrammetry on a 3D surface. It requires knowledge of the model geometry or to perform the tedious process of Cartesian model geometry reconstruction from images by using reference points on the model. It also requires positioning the camera at the exact location and angle before (for geometry reconstruction) and after running the wind tunnel (for obtaining interferograms). For example, in the NASA bump model (Naughton et al. 2006), to determine the skin-friction distribution, a grid that conformed to the model surface was applied to the model, and the model reference points image was taken. The pressure taps on the model were used with the grid positions to convert the selected grid points into the Cartesian model geometry. The grid was then removed, and the camera and light source was traversed out of the test section without changing either's orientation. Oil was then applied to the model, and the tunnel was turned on. After the test was completed, the camera and light source were traversed back into the test section to the exact location where they had taken the model reference points image, and an image of the interferogram was acquired.

In this paper, we propose a simplified procedure of OFI application on 3D surfaces with photogrammetry. We propose a technique that allows photogrammetry application on 3D surfaces without the need of knowing model geometry or conducting a tedious process of Cartesian model geometry reconstruction via reference points. Our technique allows taking images only after experiments with arbitrary camera location—without worrying about placing and measuring the camera angle and position. The proposed technique is generically applicable and would allow acquisition of benchmark skin-friction data to validate numerical simulations.

The method is first tested over a flat surface in a turbulent boundary layer flow. Then the method is employed to obtain skin friction centerline profiles over a Gaussian bump (speed bump) geometry for three freestream Mach numbers: 0.05, 0.1, and 0.2. These data are part of a series of archival benchmark validation wind tunnel experiments on smooth body TBL flow separation for CFD validation (Williams et al. 2020; Gray et al. 2021, 2022).

In the following, we present the details on the proposed method in Sect. 2. Then, in Sect. 3, we discuss the results of the method's application on a flat surface in a zero pressure gradient turbulent boundary layer and Gaussian bump geometry. Finally, concluding remarks are provided in Sect. 4.

2 Method and setup description

In this section, the procedure and the experimental setup are discussed. First, we provide the final formula to compute the skin friction following the formulation by Monson et al. (1993),

$$C_f = \frac{2n}{\lambda} \frac{\cos\theta_r \Delta x_f}{\int_0^{t_{run}} q_\infty(t)/\mu(t)dt} \quad (1)$$

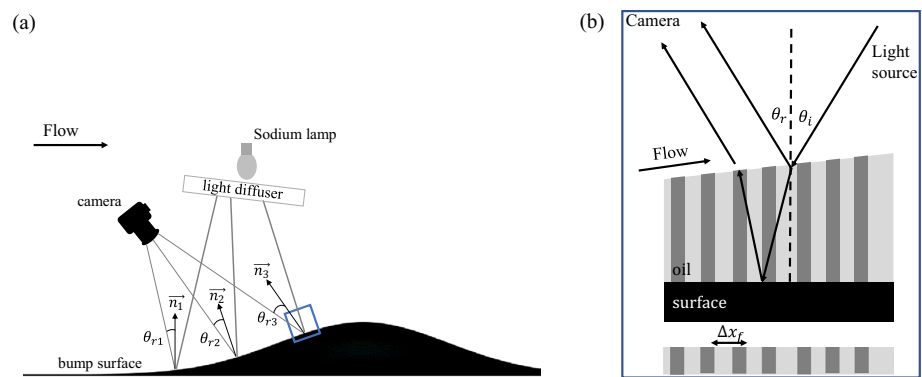
The above equation provides the relationship between the wall shear stress and the thinning of the oil-film where λ is wavelength of the monochromatic light source, n is the index of refraction of the oil, θ_r is the angle between the observation direction and the local surface normal, which is equal to the light incidence angle θ_i as illustrated in the imaging set up in Fig. 1a and Fig. 1b; Δx_f is the fringe spacing along surface streamlines, which in our case correspond to the streamwise flow direction; t_{run} is the total run time of the wind tunnel; $q_\infty(t)$ is the time variation of the dynamic pressure in the freestream flow region of test section; and $\mu(t)$ is the time variation of oil dynamic viscosity, which is a function of oil temperature during the duration of the experiment. More details on this equation can be found in Driver (2003) and its detailed derivation in Monson et al. (1993) and Naughton and Sheplak (2002).

In the following subsections, we detail the experimental procedure (Sect. 2.1), the sensor data processing obtained during the experiment (Sect. 2.2), the imaging data processing that is acquired after the experiment (Sect. 2.3), and the uncertainty analysis (Sect. 2.4) of our method.

2.1 Experimental procedure

To obtain the integral value $\int_0^{t_{run}} q_\infty(t)/\mu(t)dt$ in the denominator of Eq. (1), one should record the time history of the dynamic pressure and model temperatures during the experimental run. Whereas the value of $\cos\theta_r \Delta x_f$ in the numerator

Fig. 1 **a** Test model with imaging setup, showing the impact of surface variation on refractive angle. **b** Zoomed in view of small surface area, which highlighted by blue rectangle in panel a, demonstrating the schematic of oil-film interference process



of Eq. (1) is evaluated from the images of the resulting oil pattern after the experimental run, by using our simplified photogrammetry technique, which we describe in Sect. 2.3. Before running the wind tunnel, the following preparations are performed:

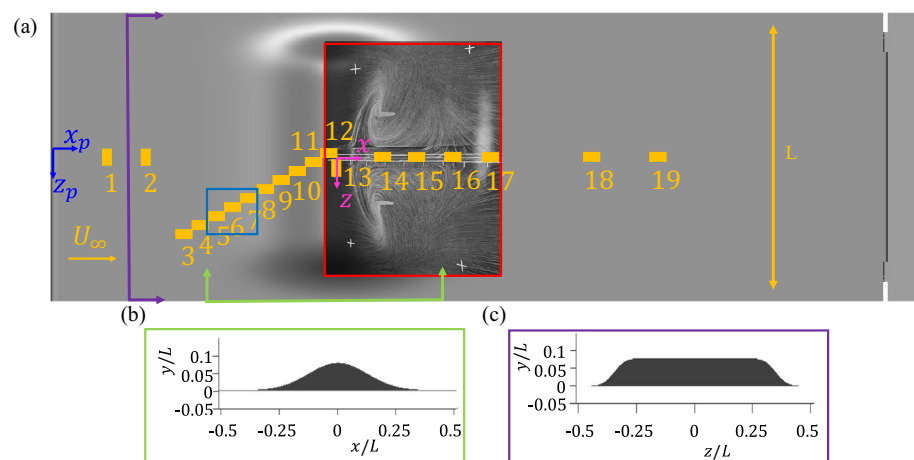
1. *Surface reflectivity adjustment*: A test surface is prepared so that it is optically smooth and reflective. A coating, such as applying thin Mylar or Kapton tape, is applied if the surface is not polished and reflective enough. If the coating reflects light with about the same intensity as the air-oil interface, a fringe pattern would be observed in the sheared oil at the end of the experiment. For more guidelines on surfaces and coating preparation for OFI, see Driver (2003).
2. *Checkerboard mounting*: A flexible small checkerboard is mounted near the oil patch. The checkerboard serves as a local calibration board, which allows one to perform our simplified photogrammetry procedure to compute $\cos\theta_r \Delta x_f$ with high accuracy.
3. *Oil application*: Select oil with viscosity based on the tunnel running conditions. The viscosity will affect

the fringe spacing at the end of the test, where less viscous oil will yield a fringe pattern with longer wavelengths. One can apply small oil patches (a small drop or line segment) at a series of locations of interest on the model surface, such that it does not run into another patch, which can destroy the resulting fringe pattern. For more guidelines on oil application for OFI, see Driver (2003).

The resulting setup after applying the three steps above is illustrated for OFI experiments over a three-dimensional speed bump geometry in Fig. 2. This bump is designed for the study of smooth body turbulent flow separation, where OFI is used for acquiring high-quality skin-friction data for the validation of ongoing computational efforts related to smooth body flow separation (Uzun and Malik 2021a, b). The three-dimensional speed bump geometry (Fig. 2) is defined by the following equation,

$$y(x, z) = \frac{h}{2} \left[1 + \operatorname{erf} \left(\frac{L}{2} - 2z_0 - |z| \right) / z_0 \right] \exp \left(-(x/x_0)^2 \right). \quad (2)$$

Fig. 2 OFI setup for Gaussian bump geometry. **a**) Top views of the bump model with apex located at $x_p = L$ (where $L = 0.914$ m) distance downstream the leading edge. The enumerated-orange-rectangle patches indicate the region where oil was applied over mounted Kapton tape square surfaces. Here, x_p denotes the bump apex location from plate's leading edge, and x denotes the streamwise location starting from bump apex. Also shown are the side view **(b)** and spanwise cross-sectional view **(c)** of bump geometry using Eq. (2)



Here $L = 0.914$ m is the model width, $h = 0.085L$ is the bump maximum height; $x_0 = 0.195L$ and $z_0 = 0.06L$ are given parameter, and x , y , and z , are streamwise, wall-normal, and spanwise spatial coordinates, respectively. The coordinate system is defined such that the center of the bump apex is located at $(0, h, 0)$ (see Fig. 2a). This geometry is also denoted simply as a Gaussian bump.

The enumerated-orange-rectangle patches in Fig. 2a, indicate the regions where oil was applied over mounted Kapton tape square surfaces. OFI measurements of skin friction have been obtained at these locations along with the centerline downstream of the bump. Whereas the uniformity of the

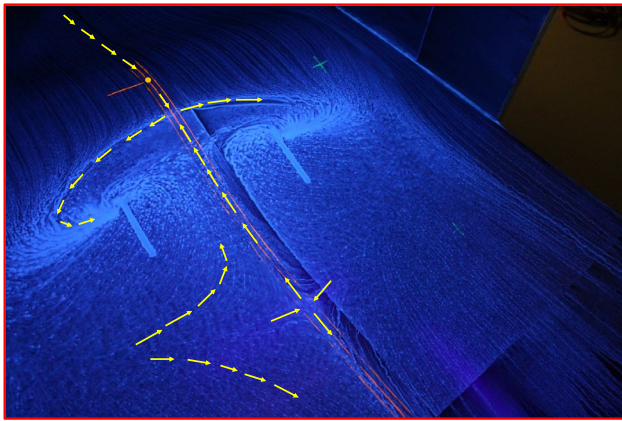
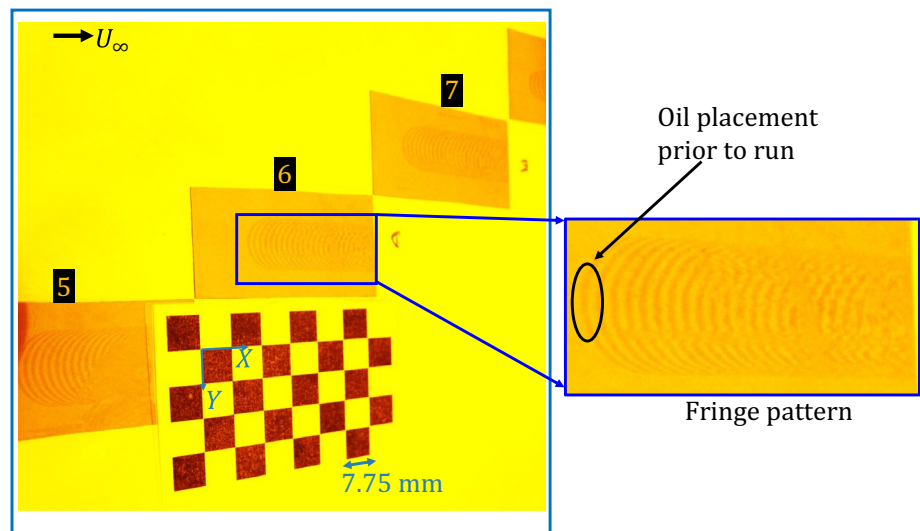


Fig. 3 Florescent oil flow visualization (for inlet freestream $U_\infty = 70$ m/s) capturing partially the flow pattern upstream (shown at top left corner of the image) and downstream the bump (in region that highlighted by red rectangle in Fig. 2a). The yellow arrows denote the streamline directions and bump apex (at $x=0$) denoted by an orange dot

streamlines upstream of the bump apex, as shown in the florescent oil flow visualization image in Fig. 3, allowed us to obtain off-span samples to resolve better the streamwise skin-friction profile upstream of the bump in a single experimental run. For more details on the oil-visualization technique over a related geometry see Williams et al. (2020); Simmons et al. (2019, 2022).

Once the setup preparations are complete, the tunnel can be closed, and the experiment started. The time histories of the dynamic pressure and model temperatures during the run are recorded. At low Mach numbers for which the aerodynamic heating of the surface is negligible, a thermocouple probe and pressure probe can be mounted in the freestream. In our study, a typical run of an experiment is about 20–30 min to allow the oil to shear and reach its final state, where 200 cSt, 1000 cSt, and 5000 cSt oil viscosities were used depending on local flow conditions, and a freestream velocity at the test section inlet was $U_\infty = 70$ m/s corresponding to $M_\infty = 0.2$. After the experiment ended, the test section was opened, and an imaging setup was installed. Our setup includes a monochromatic light source and a camera (see the illustration in Fig. 1a). At least three images of the oil pattern and checkerboard should be captured from different angles in our method, but it is important to note that it does not require documenting and measuring the camera location and orientation. One should make sure that the camera focus is zoomed out and set to manual mode to avoid autofocusing of the camera so as to maintain the same intrinsic camera parameters for each image. After running the experiment, a fringe pattern is created, as illustrated in Fig. 4. The interference pattern is captured after illuminating the surface with a sodium lamp with a wavelength of 589 nm. In this case, the images are obtained with Canon Rebel T6 camera combined with Canon EFS 18–55-mm lens.

Fig. 4 Fringe patterns after experimental run (for 200 cSt oil, 20-min run, inlet freestream $U_\infty = 70$ m/s, which correspond to $M_\infty = 0.2$) at locations 5–7 in the highlighted blue rectangle region in Fig. 2a and nearby checkerboard (7.75 mm square size), where we denote its pattern local X-Y coordinate system



2.2 Sensor data processing

To obtain the integral value $(\int_0^{t_{run}} q_{\infty}(t)/\mu(t)dt)$ in the denominator of Eq. (1), we evaluate the time history of $\mu(t)$ (Pa s). In our study, we used Clearco oils, for which the computational expression (curve fit) that was provided in Clearco's viscosity-to-temperature charts data sheet is given by, (see details in Simmons (2020)),

$$\mu(T(t)) = \rho 10^{\left(-6 + \frac{763.1}{273.16+T} - 2.559 + \log(v_0)\right)}. \quad (3)$$

Here ρ and v_0 are oil density (kg/m^3) and oil dynamic viscosity (cSt), respectively, both at 25 °C. Three Clearco oils were used with different properties. The first having $v_0 = 200$ cSt, $n = 1.4026$, and $\rho = 969$ kg/m^3 ; the second was more viscous having $v_0 = 1000$ cSt, $n = 1.4031$, and $\rho = 974$ kg/m^3 , and we also tested with a high viscosity oil having $v_0 = 5000$ cSt, $n = 1.4035$, and $\rho = 975$ kg/m^3 . A K-type thermocouple was used to obtain temperature readings for these experiments sampled at 10 Hz.

2.3 Image processing with simplified photogrammetry

The images that capture the checkerboard with the nearby fringe pattern are used to accurately obtain the $\cos\theta_r \Delta x_f$ term in the numerator of Eq. (1). Our simplified photogrammetry technique employs camera calibration algorithms for estimating camera intrinsic, extrinsic, and distortion parameters to obtain accurately θ_r and Δx_f , without any a-priori knowledge of the surface geometry and camera position. In particular, we use a set of functions that are available in the Computer Vision Toolbox in MATLAB R2020a. The procedure steps are as follows:

1. Estimate Camera Parameters (Calibration).

- i. Detect a checkerboard pattern in a set of input images.
- ii. Generate the *world coordinates* of the checkerboard corners.
- iii. Set *pattern local X – Y coordinate system* with the upper-left corner at (0,0).
- iv. Estimate intrinsic and extrinsic parameters and the distortion coefficients.
- v. Evaluate standard estimation errors for the single camera calibration.

2. Select single image.

- i. Remove lens distortion from the image.

- ii. Detect the checkerboard in the selected undistorted image.
- iii. Compute rotation and translation of the camera with respect to the checkerboard in that image.

3. Select localized area in the fringe pattern in the image.

- i. Segment fringes and compute their average spacing Δx_f in that area.
- ii. Compute the camera refraction angle θ_r to the center of the fringe area.

In the first and second steps above, a set of multiple images (at least 3) of a calibration pattern is obtained from different angles. A typical calibration pattern is an asymmetric checkerboard, that contains an even number of squares along one side, and odd number of squares along the other. The size of a square must be measured in world units as precisely as possible. The asymmetric checkerboard allows one to define a *pattern local X – Y coordinate system* with the upper-left corner at (0,0) in the detected checkerboard pattern, where X is the direction along the long side, and Y is the direction along the short side, as shown on the checkerboard in Fig. 4.

Camera calibration estimates the values of the intrinsic parameters, the extrinsic parameters, and the distortion coefficients. The extrinsic parameters represent a rigid transformation from the 3D world coordinate system to the 3D camera's coordinate system. The intrinsic parameters represent a projective transformation from the 3D camera's coordinates into the 2D image coordinates. The calibration algorithm assumes a pinhole camera model, where the following system is solved

$$w \begin{bmatrix} x_i & y_i & 1 \end{bmatrix} = \begin{bmatrix} X & Y & Z & 1 \end{bmatrix} \begin{bmatrix} \mathbf{R} \\ \mathbf{t} \end{bmatrix} \mathbf{K}. \quad (4)$$

Here, (X, Y, Z) are the *world coordinates* (metric units, like the one we define in Fig. 4) of a point; (x_i, y_i) coordinates (pixel plane of the image) of the corresponding image point; w : arbitrary scale factor. The world points are transformed to camera coordinates using the extrinsic parameters consisting of \mathbf{R} , the 3D rotation matrix of the camera and \mathbf{t} , the translation of the camera relative to the world coordinate system. The camera coordinates are mapped into the image plane using the intrinsic parameters within camera intrinsic matrix \mathbf{K} that is defined as:

$$\mathbf{K} = \begin{bmatrix} f_x & 0 & 0 \\ s & f_y & 0 \\ c_x & c_y & 1 \end{bmatrix}, \quad (5)$$

where $[c_x, c_y]$ is the optical center (the principal point), in pixels; (f_x, f_y) -focal length in pixels; and s is the skew coefficient.

The system in Eq. 4 does not account for lens distortion because an ideal pinhole camera does not have a lens. However, the camera model should also include the radial and tangential lens distortion to represent a real camera accurately. Radial distortion occurs when light rays bend more near the edges of a lens than they do at its optical center. The smaller the lens, the greater the distortion, whereas tangential distortion occurs when the lens and the image plane are not parallel. A number of radial distortion coefficients and tangential distortion coefficients can be defined and then estimated for calibration. For more details on these distortions, see Chari and Veeraraghavan (2014). Therefore, two steps are involved in camera calibration to account for these types of distortions. First, the system in Eq. 4 is solved for the intrinsics and extrinsics in closed form, assuming that lens distortion is zero (Zhang 2000). Then, estimate all parameters simultaneously, including the distortion coefficients using nonlinear least-squares minimization (Levenberg-Marquardt algorithm) (Zhang 2000; Heikkilä and Silvén 1997). These steps are employed in our study by using built-in MATLAB calibration algorithms, which can also provide the calibration accuracy.

We first illustrate the obtained camera calibration using a checkerboard mounted on a flat plate surface. Figure 5a shows the result of four input images of a simple printed array of black and white squares each with size 5.67 mm. The detected calibration pattern allows evaluation of extrinsic parameters from which one can obtain the camera location and orientation with respect to each image as shown in Fig. 5b. The estimated errors are shown in Fig. 5c. The bar graph indicates the accuracy of the calibration, where each bar shows the mean reprojection error for the corresponding calibration image. The reprojection errors are the distances between the corner points detected in the image and the corresponding world points projected into the image.

The calibration assumes that the checkerboard is as flat as possible. Thus, it estimates the lens distortion and other camera intrinsics that would yield an undistorted image showing a flattened checkerboard. Then, the estimated intrinsic parameters are used to remove the resulting distortion. In Fig. 5d, we show the resulting undistorted image of the fourth image in Fig. 5a. One can see that the undistorted image is slightly modified to yield a flat checkerboard.

In the case of applying the checkerboard on a curved surface, the calibration procedure would still assume that the checkerboard is as flat as possible. We exploit this for obtaining the camera angle to the surface and correct

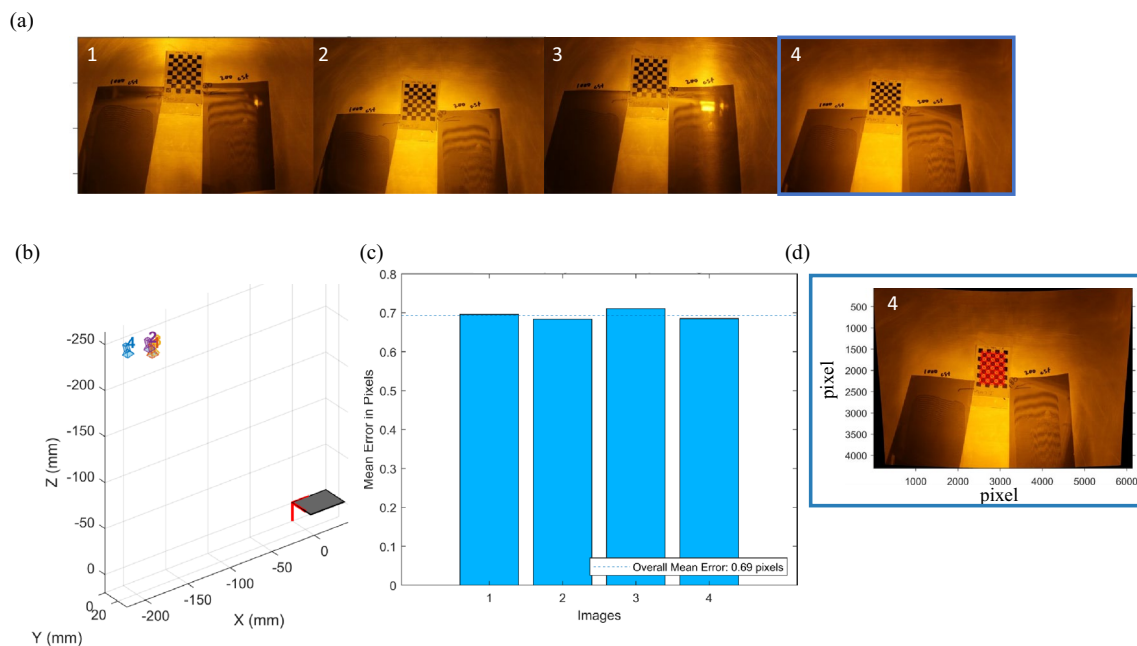


Fig. 5 Calibration procedure illustration on a flat surface. **a** Set of four images with a checkerboard pattern (5.67 mm square size). **b** Extrinsic parameters visualization, where the camera for each image is projected in space relative to the local origin of the calibration

board. **c** Mean projected error per image. **d** Undistorted image (of the fourth image in the provided image set in panel a) with the detected checkerboard

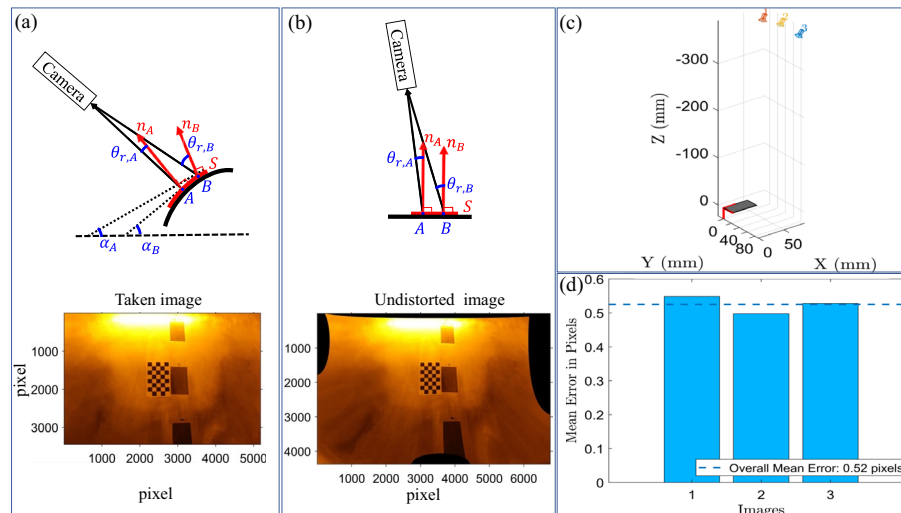


Fig. 6 Undistorting image process for checkerboard over a curved surface (illustrated for placing the checkerboard over the Gaussian bump near enumerated-orange-rectangle number 14 in Fig. 2a): **a** the camera angle with respect to the deformed checkerboard (red curve) mounted on the curved surface (black curve). Here, α_A and α_B represent the angles to the horizontal line of the local surface slope, with

distances between the fringes accurately for any curvature. This process is illustrated in Fig. 6a and Fig. 6b for placing the checkerboard over the Gaussian bump near enumerated-orange-rectangle number 14, whose location is shown in Fig. 2a. Figure 6a shows that the angle θ_r will be different at different points on the surface ($\theta_{r,A}$ and $\theta_{r,B}$) due to both camera distance and surface geometry curvature. This, in turn, would require knowing the surface geometry and camera position, and orientation. However, our method relaxes these requirements. The idea is that mounting the flexible checkerboard firmly to the surface would deform the checkerboard (Fig. 6a), which in turn allows us to establish the relation from images to coordinates of the surface. Therefore, the calibration algorithm would identify the deformation of the checkerboard and would yield an undistorted image in an attempt to flatten the checkerboard and thus unfold the curved surface (Fig. 6b). The camera intrinsics and lens distortion effect can be isolated from the surface curvature effect by calibrating the camera beforehand using a checkerboard on a flat surface, but typically the distortion due to the camera lens is negligible compared to surface curvature, and this step can be skipped. The undistorted image yields a flattened checkerboard, and thus, the surface coordinate is mapped to the Cartesian coordinate, allowing one to obtain the correct distances between the fringes Δx_f that follow the surface curvature and evaluate the angle θ_r correctly with respect to the unfolded surface normal to any point in the closed environment to the checkerboard. Therefore, the determination of θ_r to any point on the image is straightforward, using only camera extrinsic information, without the need for surface

the corresponding surface normal \hat{n}_A and normal \hat{n}_B , at points A and B, respectively. S denotes the arc length of the red curve along the surface. **b** The process of calibration deforms the image to flatten the checkerboard. **c** Extrinsic parameters visualization, where the camera for each image is projected in space relative to the local origin of the calibration board. **c**) Mean projected error per image

geometry. In our case, a checkerboard with a square size of 7.75 mm is used, and three images are obtained. Comparing the undistorted images between Fig. 5d with a checkerboard on a flat surface and Fig. 6b with a checkerboard on a curved surface shows that the contribution of lens distortion compared to surface curvature is not significant. Also shown is a result of calibration with three images for the curved surface, where we show the obtained extrinsics in Fig. 6c and their corresponding error in Fig. 6d. One can clearly see that the estimation of extrinsic parameters, which are needed for accurate determination of θ_r , is not deteriorated due to the surface curvature. Similarly in Naughton et al. (2006) who employed OFI coupled with photogrammetry procedure over a NASA hump model, it was found that θ_r is not very sensitive to these properties of camera/lens system intrinsic and distortion, and thus they skip the camera calibration step. Moreover, we consistently obtained good agreement between the estimated camera extrinsics with respect to the physical camera location/orientation measurements for both flat and curved checkerboard tests.

After completing the first two steps—image calibration and undistorting the selected image—a third step can be performed. In this step, we compute the angle θ_r to the center of the fringe region rectangle and evaluate the fringe spacing via segmentation. Average skin friction would be obtained for that area. Therefore, one should ensure that the interference fringes are uniform throughout that region. The smaller the area, the more localized skin friction we get; however, it should be large enough that at least two fringes are captured. The fringes in the selected rectangle are segmented

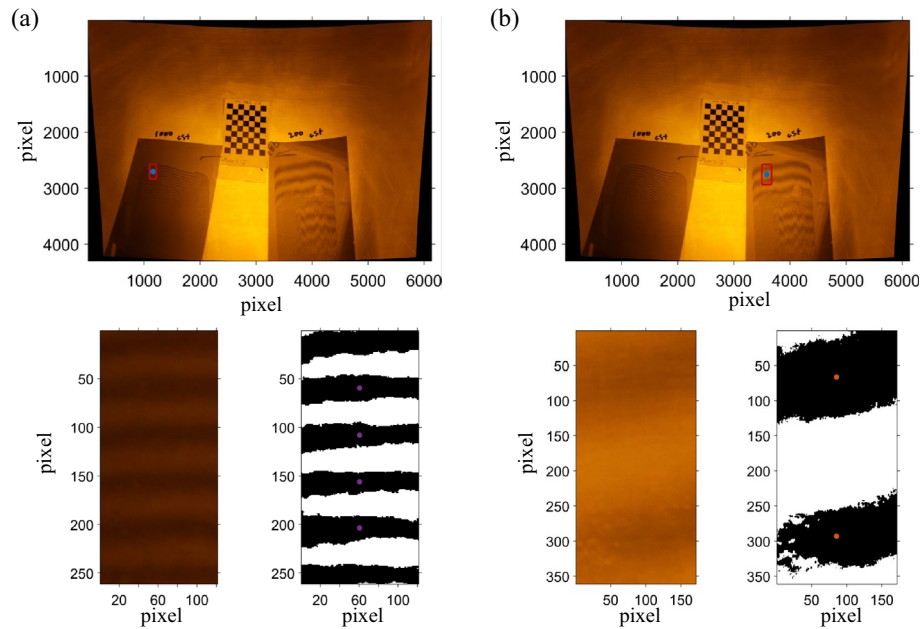


Fig. 7 Undistorted image of OFI application on a flat plate at $x = 486$ mm region (checkerboard origin) after a 20-min run at $M_\infty = 0.2$. For this case, a checkerboard with a square size of 5.67 mm was used. Two oil patches at different viscosities were applied at each checkerboard span sides. **a** Selected fringe region (red rectangle frame with 13.57 mm of its long side) over fringe pattern for 1000 cSt oil and obtained $\Delta x_f = 2.502$ mm, $\theta_r = 39.91$, and $c_f = 2.676 \times 10^{-3}$.

b Selected fringe region (red rectangle frame with 19.43 mm of its long side) over fringe pattern for 200 cSt oil and obtained $\Delta x_f = 12.275$ mm, $\theta_r = 38.13$, and $c_f = 2.681 \times 10^{-3}$. The resulting segmented fringes in the selected rectangle region are shown for each oil below the undistorted image. The angle is computed to the rectangle center, which denoted by blue asterisk symbol

to evaluate the fringe spacing. We do so via converting the image to HSV (hue, saturation, value) color space and getting a saturation channel. Then a threshold, using the *graythresh* function in MATLAB that employs Otsu's method

(Otsu 1979), is set in order to produce a binary fringe pattern. The process is illustrated in Fig. 7, where two oils with different viscosities (200 cSt and 1000 cSt) are applied on a flat plate at 486 mm downstream of the plate leading edge.

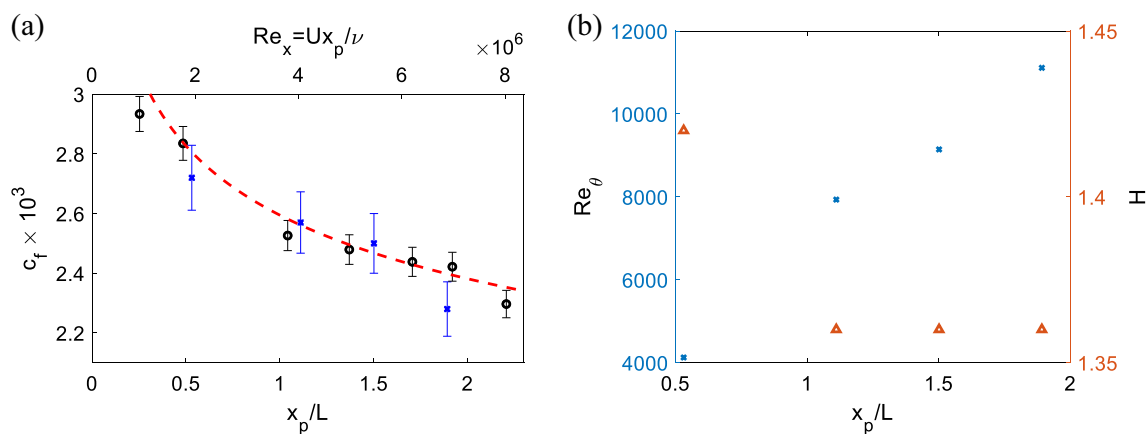


Fig. 8 **a** Clauser c_f values (blue cross symbols, with 4% error bars) and OFI c_f values (black circle symbols with 2% error bars) for TBL at a test section inlet freestream Mach number of $M_\infty = 0.2$. In this plot, x_p denotes the streamwise location from the splitter plate's leading edge. A red dashed curve denotes a power-law fit ($c_f = 0.017 Re_x^{-0.1237}$) to skin friction coefficient measurements

obtained by Oweis et al. (2010) for a smooth-flat-plate turbulent boundary layer at a high Reynolds number, using the flush-mounted floating-plate force balances. **b** Boundary layer parameters: momentum-thickness Reynolds number, Re_θ (blue cross symbols), and shape factor, H (orange triangle symbols), at locations where boundary layer profiles are obtained for Clauser method

The plate had trip dots placed 51 mm downstream the leading edge (with 2.5 mm spacing, where each dot height is 0.292 mm, and diameter 1.27 mm), which yielded a fully developed TBL (shape factor equal to 1.37 as illustrated in Fig. 8b) in that region. After running, the tunnel for 20 min at freestream Mach $M_\infty = 0.2$, images of the resulting fringe pattern were taken. One can see the 200 cSt oil sheared over a larger distance than 1000 cSt, which yields fewer fringes in the rectangular area. To increase the accuracy of the fringe spacing evaluation, we evaluated the distance between the fringes for each column of pixels in the rectangle and averaged it. More fringes along the span would yield more data to be averaged, thus reducing the error. After these steps, one can compute the skin friction using the obtained sensor and imaging data. The procedure yields nearly the same value of the skin friction for both oil viscosities ($c_f = 2.676 \times 10^{-3}$ for 1000 cSt oil and $c_f = 2.681 \times 10^{-3}$ for 200 cSt oil), demonstrating the robustness of our method.

2.4 Uncertainty

There is a vast literature dealing with uncertainty analysis in OFI (such as Hubner and Carroll 1991; Zilliac 1996; Segalini et al. 2015; Rezaeiravesh et al. 2018; Lee et al. 2019). In particular, a summary of error sources and their estimated value on OFI can be found in (table 2, Zilliac 1996), whereas a detailed uncertainty quantification via mathematical and statistical approaches to identify the parameters of the highest impact on the overall uncertainty to OFI was done by Rezaeiravesh et al. (2018). In addition, a propagation of the uncertainties of each of the parameters in Eq. (1) for our setup is detailed in Simmons (Section D.4 2020). Herein, we only discuss the dominant uncertainties.

We consider two categories of uncertainties: probabilistic and systematic. The probabilistic errors are uncertainties that are considered to be independent of each other and can occur due to noise, fringe visibility, surface imperfections, variations in the illumination on the surface, and also uncertainty as a result of a departure from the assumptions that are used to obtain Eq. (1), such as two-dimensionality of the thin layer. One way to reduce these error impacts is to evaluate hundreds of individual c_f values at the same location, which would lead to an average c_f with a small precision error. For example, see Naughton et al. (2003, Figure 10), Naughton et al. (2006, Figure 10), where the total uncertainty was determined by summation in the rms sense, showing its decrease with an increasing number of samples. In our study, to increase the accuracy of the fringe spacing evaluation, we evaluated the distance between the fringes for each column of pixels in the rectangle (at least 100 columns were used in our study) and averaged it. More M independent measurements of fringes along the span would yield more data to

be averaged, thus reducing the random error e_r by a factor of \sqrt{M} , i.e., e_r/\sqrt{M} . However, this procedure cannot help with systematic errors.

In our study, two factors contribute the most to the overall systematic error in wall-shear stress measurements: the estimated incident camera angle and the variation in the oil viscosity as a function of temperature measurement. The results indicate that when model curvature is high, or the camera-to-model distance is short, significant uncertainties of the order of 10% in skin friction can be introduced due to angle bias if photogrammetry is not applied (Naughton and Liu 2007; Naughton et al. 2006). In our study, 1 degree in angle error would lead to 0.88% error in skin friction. With the photogrammetry technique employed here, we can estimate the angle to every pixel in the image that varies below 0.2° in the selected rectangle of interest, thus reducing the error to be negligible. In that regard, the uncertainty caused by the photogrammetry was found to be, in most cases, significantly less than the other uncertainties (Naughton and Liu 2007; Naughton et al. 2006). An additional uncertainty related to our technique is that the checkerboard curvature is not the same as the curvature where we measure the fringe pattern. In our case, we made sure that the checkerboard was sufficiently small and placed along the span where the fringes are taken with uniform curvature captured by the checkerboard. Difficulties may arise in measuring skin friction value on 3D bump regions with high curvatures (e.g., the apex region), where greater care on checkerboard size selection and mounting location should be taken.

The remaining source of error is the viscosity variation with temperature, where propagation analysis yields that for every degree Celsius error, the calculated shear stress obtains a 1.8% error. In our case, we used K-type calibrated thermocouple, where calibration assured that its accuracy is within 0.5°C .

Lastly, nonconstant run conditions can be an additional leading source of error, with tunnel startup and shutdown transients producing different flow conditions from the desired test condition. A conservative estimate of skin-friction uncertainty is to assume that the uncertainty is proportional to the ratio of time spent in startup and shutdown relative to the total run time (Driver 2003). Thus, to make it negligible in our analysis, we run 20-min duration experiments, whereas the startup time with added shutdown time took less than 40 s (3.33% of total run time) for the Mach 0.2 experiments, which lead to uncertainty of 0.7% (overprediction) to the overall error in c_f in our experiments.

To conclude, the overall bias error in mean skin-friction values is taken to be within 2%, assuming that the oil was calibrated with the uncertainty of 0.2% of ν_0 , and an oil temperature uncertainty of 0.5°C . The uncertainties due to initial oil conditions, light source wavelength variations, oil index of refraction variations, pressure gradients, and tunnel

startup and shutdown effects have been neglected because they were considered too small to significantly impact the total uncertainty of the c_f measurements.

3 Results

In this section, we show results of the application of the method in evaluating skin friction for two cases. First, we compare the skin-friction values determined using our OFI method with the Clauser method in a fully developed zero pressure gradient TBL over a flat surface. Second, an experiment is performed on a Gaussian bump geometry. This geometry provides significant challenges due to model curvature and camera proximity.

3.1 Turbulent boundary layer

The log-law fitting method of Clauser (1956) was implemented on the hot-wire boundary layer mean velocity profiles to compare the skin friction values obtained by our OFI method for the canonical nominally zero pressure gradient (flat plate) TBL. The normal wall position of the probe was controlled with a stepping resolution of 5 microns. Kapton tape of 1 mil (0.0254 mm) thickness was placed on the wall at each hot-wire TBL profile location to reduce wall heat conduction near the surface. The same Kapton tape was also utilized as a reflective surface for our OFI procedure. More details on the experiment and a detailed example of the aforementioned Clauser method applied to a boundary layer profile at $x_p = 1.02$ m, downstream of the plate leading edge, are provided in Gray et al. (2021).

In Fig. 8a, we show skin friction, c_f , values obtained via the Clauser method evaluated at $M_\infty = 0.2$ for the TBL mean velocity profiles at $x_p = 0.49$ m, 1.02 m, 1.37 m, and 1.73 m. These are compared to the c_f values obtained with the OFI data, where experimental conditions and the OFI procedure provided in previous Section 2.3 are utilized for Fig. 7. In addition, we show on the same plot a solid curve that is obtained from a least-squares power-law fit, $c_f = 0.017 Re_x^{-0.1237}$ where $Re_x = U_\infty x_p / \nu$, to skin-friction measurements obtained by Oweis et al. (2010) over a flat plate in a water tunnel. We also show in Fig. 8b the momentum-thickness Reynolds number, Re_θ , and shape factor, H , at locations where boundary layer profiles are obtained for the Clauser method. The shape factor is approximately 1.42 at the $x_p = 0.49$ m location and drops to 1.36—a value within range (1.3–1.4) expected for a zero pressure gradient turbulent boundary—farther downstream once the TBL fully develops from the tripped leading edge. More details on the characterization of splitter plate and incoming boundary

layer for $M_\infty = 0.2$ ($U_\infty = 70$ m/s) are provided in Gray et al. (2021) and for lower speeds ($U_\infty = 20 - 60$ m/s) in Williams et al. (2020). Figure 8a shows good agreement between the two methods along the streamwise distance of the flat splitter plate. Good agreement is also obtained with the power-law fit within the experimental uncertainty of Williams et al. (2020), accounting for the difference between the setups, such as the model's elliptical leading edge and boundary layer trip location affecting the virtual origin used in determining Re_x . The similarity between data sets from the different techniques establishes confidence in the OFI technique and motivates its application for the more complex Gaussian bump geometry.

Moreover, the friction velocity $u_\tau \equiv \sqrt{\tau_w / \rho}$, which relates directly to the surface shear stress τ_w , is an important parameter that is extensively used for scaling of the TBL in viscous or wall units. Small errors in estimating u_τ would lead to significant errors in shear stress analysis. It is not always possible to determine the friction velocity u_τ by adjusting u_τ value until this curve passes through the log law. Moreover, it provides an accuracy of approximately 1 %–4 % for turbulent smooth and rough-wall boundary layer with techniques that account for small pressure gradients (Womack et al. 2019). In the case of pressure gradients presence, such as in turbulent separated flows, the most accurate way is determining the shear stress using oil-film interferometry, where u_τ can be obtained from

$$u_\tau = U_\infty \sqrt{\frac{c_f}{2}}. \quad (6)$$

3.2 Gaussian bump model

The OFI measurements were taken in the Mach 0.6 closed-loop wind tunnel at the University of Notre Dame. The OFI setup for these tests is shown in Fig. 2 and described in Sect. 2 for $M_\infty = 0.2$, and in Gray et al. (2022). In these tests, we obtained the streamwise variation of skin friction over Gaussian bump geometry along its centerline for two bump locations: bump apex at $x_p/L = 1$ and $x_p/L = 2$, where x_p denotes streamwise location from the boundary layer development-plate leading edge (see Fig. 2a), where the plate was suspended at the midheight of the test section. At each bump location, we collected data for three flow regimes at $M_\infty = 0.05, 0.1$, and 0.2, for which the corresponding Reynolds number (based on tunnel width) is: $Re_L = U_\infty L / \nu = 1 \times 10^6, 2 \times 10^6$ and 4×10^6 , respectively, where $\nu = 1.61 \times 10^{-5} \text{ m}^2/\text{s}$. Overall, we obtained six centerline skin-friction profiles. The obtained results are shown in Figs. 9a–d.

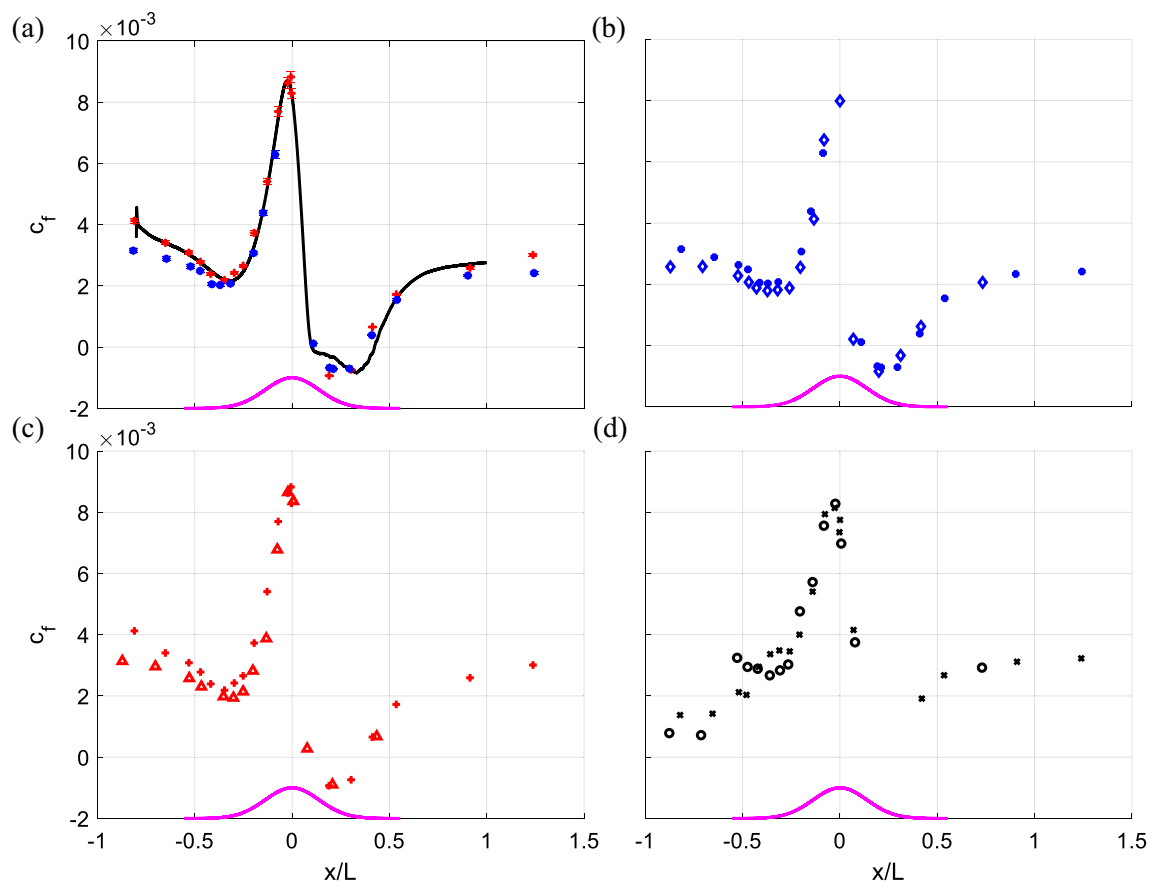


Fig. 9 Skin-friction distributions over the bump geometry: **a** DNS and OFI data for bump apex at $x_p/L = 1$: and for DNS (M_∞, Re_L) = (0.2, 2×10^6) (black curve); OFI data at (M_∞, Re_L) = (0.1, 2×10^6) (red plus symbols with 2% error bars); and OFI data at (M_∞, Re_L) = (0.2, 4×10^6) (blue dot symbols with 2% error bars). DNS curve reproduced from data provided by the authors of Uzun and Malik (2021a) with permission from the authors and AIAA. **b** OFI data at (M_∞, Re_L) = (0.2, 4×10^6):

for $x_p/L = 1$ (blue dot symbols) and $x_p/L = 2$ (blue diamond symbols). **c** OFI data at (M_∞, Re_L) = (0.1, 2×10^6): for $x_p/L = 1$ (red plus symbols) and $x_p/L = 2$ (red triangle symbols). **d** OFI data at (M_∞, Re_L) = (0.05, 1×10^6): for $x_p/L = 1$ (black cross symbols) and $x_p/L = 2$ (black circle symbols). In all panels, the bump profile is denoted by magenta curve. Here, x_p denotes the bump apex location from plate's leading edge, and x denotes the streamwise location starting from bump apex

In Fig. 9a, our data are plotted vs DNS simulation (Uzun and Malik 2021a, b) for the same bump geometry where $M_\infty = 0.2$ and the bump apex is located at $x_p/L = 1$. However, the DNS Reynolds number for $M_\infty = 0.2$ is $Re_L = 2 \times 10^6$, whereas in our case we obtain $Re_L = 4 \times 10^6$ for the same Mach number. To address this discrepancy, both experimental runs—for $M_\infty = 0.1$ (that match simulation Reynolds number) and 0.2 (that match simulation Mach number)—were compared to the DNS profile. Figure 9a shows that the DNS data agree better with the experimental case with (M_∞, Re_L) = (0.1, 2×10^6) at the boundary layer development plate surface upstream the bump than for (M_∞, Re_L) = (0.2, 4×10^6), indicating the importance of approach boundary layer thickness to the skin-friction values, which is obtained by matching the Reynolds number to DNS data. In that region, beginning near the leading edge of the plate, the skin-friction values are decreasing toward the bump.

For other regions—just upstream of the bump, on, and downstream the bump—both experimental cases yield very similar skin-friction profiles. In these regions, at a closer distance to the upstream portion of the bump, the effect of the favorable pressure gradient accelerates the flow, and an increase in skin friction is evident until about $x/L = -0.05$, where a primary c_f peak is obtained. At this point (the exact location needs to be resolved in more detail and is subject to further investigation), the c_f curve begins to drop quickly. Downstream of the bump apex, negative c_f values were acquired in the separated flow region, where a reverse oil flow pattern is observed (for example, see the surface oil visualization image attached to the plate in Fig. 2a and in Fig. 3). From this region, the experimental data begin to deviate from the DNS slightly. The DNS curve seems to miss the lower peak that is captured by both of the experiments near $x/L = 0.2$. This may be associated with the presence of moderate three-dimensionality effects even at

the centerline of the model (Williams et al. 2020), which are not fully captured in the DNS simulation that assumes spanwise periodicity (Uzun and Malik 2021a). The boundary layer then reattaches at $x/L = 0.4$ (where the mean wall shear stress is zero) and begins to recover. The difference between experimental cases in the far wake (for $x/L > 1$) is also evident, where we assume that the boundary layer thickness is different for each case after the reattachment point and this plays a key role in the flow physics (this will be validated in our future studies via detailed flow field characterization experiments).

The importance of boundary layer thickness on the skin-friction distribution upstream the bump is emphasized in Figs. 9b–d, where we keep the (M_∞, Re_L) pair the same, but place the bump at two different downstream locations along with the development plate at $x_p/L = 1$ and $x_p/L = 2$. For Fig. 9b and Fig. 9c a fully developed turbulent boundary layer was documented for $(M_\infty, Re_L) = (0.2, 4 \times 10^6)$ and $(0.1, 2 \times 10^6)$ flow regimes, respectively, at the development plate region upstream of the bump. In such a case, moving the bump locations farther downstream would increase the Reynolds number based on boundary layer (integral) scaling (as shown in Fig. 8b for Re_θ). Increased thickness yields lower skin-friction values upstream the bump apex. In the case of $(M_\infty, Re_L) = (0.05, 1 \times 10^6)$, the profile departs from other skin-friction profiles that were obtained for higher freestream velocities, where a kink is observed at $x/L = -0.5$ (upstream the bump), which was also evident from surface pressure profiles in Williams et al. (2020) for this speed. It can be associated with partial relaminarization of the flow on the upstream face of the bump, which is discussed in detail in (Uzun and Malik 2021b), with additional phenomena such as stabilization in the strong acceleration region, retransition to turbulence near the onset of adverse pressure gradient, incipient/weak separation, and development of internal layers where the sense of streamwise pressure gradient changes at the foot, apex, and tail of the bump. Our OFI results can complement and validate simulation studies to examine these key phenomena in the flow field over complex geometries.

4 Conclusions

A simplified procedure of OFI application on 3D surfaces with photogrammetry is presented. Photogrammetry is vital for accurate quantitative skin-friction measurements over curved surfaces and at different oil flow imaging settings. It is needed to accurately determine the local incidence angle at each point in the interferogram and fringe spacing. However, it requires information on surface geometry and placing the camera in the exact location and orientation before and after the wind-tunnel run, which complicates the simplicity of OFI.

Herein, we propose and demonstrate a technique that allows photogrammetry application on 3D surfaces without

a priori knowledge of model geometry or conducting a tedious process of Cartesian model geometry reconstruction via reference points. Our technique allows taking images after experiments with arbitrary camera location and without the need to place and measure the camera angle and position.

Removal of these constraints may allow assessing mean skin friction over air-vehicle fuselage at different locations which otherwise would be very elaborate and challenging with traditional photogrammetry requirements.

The method is based on OFI measurements coupled with photogrammetry that we simplified via exploiting camera calibration algorithms and applying a small flexible checkerboard near the fringe pattern. Mounting a checkerboard on the surface of the curved surface deforms the square pattern, which in turn allows determining the surface curvature distortion during the calibration process. In turn, it allows accurately determining the fringe spacing and the camera incident angle to the curved surface.

The method was tested on a flat plate with zero pressure gradient turbulent boundary flow where good agreement is demonstrated with the Clauser method. Our technique is beneficial in obtaining the friction velocity, which is an important parameter that is extensively used for scaling of the TBL in viscous or wall units where small errors in estimating friction velocity would lead to significant errors in shear stress analysis. The method is subsequently employed to obtain the skin-friction centerline streamwise distributions over a Gaussian bump geometry for three freestream Mach numbers: 0.05, 0.1, and 0.2, which is a part of a series of archival benchmark CFD validation wind tunnel experiments on smooth body TBL flows leading to separation. We show good agreement with DNS data and show with our method the importance of boundary layer thickness on skin-friction profile upstream the bump, where increased thickness yields lower skin-friction values.

Our method is suggested to complement and validate simulation studies to examine key phenomena in the flow field over complex geometries. In future studies, we will examine extending the suggested algorithm for global OFI measurements (over certain regions rather than at discrete points on the surface). This can be achieved through obtaining near-surface streamlines on the 3D model's surface and computing the skin friction along these streamlines. The streamlines should be mapped correctly on the model, and future efforts will focus on that task.

Acknowledgements This work is funded through the Office of Naval Research (ONR) Cooperative Agreement No. N00014-20-2-1002, between ONR, the Boeing Company, the National Aeronautics and Space Administration, the Army Research Lab, the Air Force Research Lab. Boeing makes no representation or warranty of any kind to the Publisher or any other person or entity regarding the Work, the information contained therein, or any related copyright.

Declarations

Conflict of interest The authors have no competing interests to declare that are relevant to the content of this article.

Consent for publication Boeing is willing to assign its copyright in the Work to Publisher subject to the limitations set forth below: 1. Any rights granted by Boeing to the Publisher are limited to the work-made-for-hire rights Boeing enjoys in the Work. 2. Boeing retains a nonexclusive, perpetual, worldwide, royalty-free right, without restriction or limitation, to use, reproduce, publicly distribute, display, and perform and make derivative works from the Work, and to permit others to do so.

References

- Baldwin A, Mears LJ, Arora N, Kumar R, Alvi FS, Naughton JW (2019) Skin friction measurements using oil film interferometry in a 3-d supersonic flowfield. *AIAA J* 57(4):1373–1382
- Bourassa C, Thomas F (2009) An experimental investigation of a highly accelerated turbulent boundary layer. *J Fluid Mech* 634:359–404
- Chari V, Veeraraghavan A (2014) Lens distortion, radial distortion. Springer, Boston, pp 443–445
- Clauser FH (1956) The turbulent boundary layer, *Advances in applied mechanics*, vol 4. Elsevier, London, pp 1–51
- Dong H, Liu S, Geng X, Cui Y, Khoo B (2018) A note on flow characterization of the fx63-137 airfoil at low reynolds number using oil-film interferometry technique. *Phys Fluids* 30(10):101701
- Driver DM (2003) Application of oil-film interferometry skin-friction measurement to large wind tunnels. *Exp Fluids* 34(6):717–725
- Gray PD, Gluzman I, Thomas F, Corke T, Lakebrink M, Mejia K (2021) A new validation experiment for smooth-body separation. In *AIAA Aviation 2021 Forum*, pp 2810
- Gray PD, Gluzman I, Thomas F, Corke T, Mejia K (2022) Experimental characterization of smooth body flow separation over wall-mounted gaussian bump. In *AIAA SCITECH 2022 Forum*, pp 1209
- Heikkilä J, Silvén O (1997) A four-step camera calibration procedure with implicit image correction. In *Proceedings of IEEE computer society conference on computer vision and pattern recognition*, pp 1106–1112. IEEE
- Hubner JP, Carroll BF (1991) Uncertainty analysis on thin-oil-film skin friction measurements in compressible flow. In *ICIASF'91 Record., International Congress on Instrumentation in Aerospace Simulation Facilities*, pp 231–239. IEEE
- Lee T, Nonomura T, Asai K, Naughton JW (2019) Validation and uncertainty analysis of global luminescent oil-film skin-friction field measurement. *Meas Sci Technol* 31(3):035204
- Liu T (2019) Global skin friction measurements and interpretation. *Progress Aerospace Sci* 111:100584
- Liu T, Burner AW, Jones TW, Barrows DA (2012) Photogrammetric techniques for aerospace applications. *Progress Aerospace Sci* 54:1–58
- Liu T, Cattafesta L III, Radeztsky R, Burner A (2000) Photogrammetry applied to wind-tunnel testing. *AIAA J* 38(6):964–971
- Lunte J, Schüle E (2020) Wall shear stress measurements by white-light oil-film interferometry. *Exp Fluids* 61(3):1–12
- Mateer GG, Monson DJ, Menter FR (1996) Skin-friction measurements and calculations on a lifting airfoil. *AIAA J* 34(2):231–236
- Monson DJ, Mateer GG, Menter FR (1993) Boundary-layer transition and global skin friction measurement with an oil-fringe imaging technique. *SAE Transact* 102:1829–1843
- Nagib HM, Christophorou C, Monkewitz PA (2006) High reynolds number turbulent boundary layers subjected to various pressure-gradient conditions. In *IUTAM symposium on one hundred Years of boundary layer research*, pp 383–394. Springer
- Naughton J, Hind M (2013) Multi-image oil-film interferometry skin friction measurements. *Meas Sci Technol* 24(12):124003
- Naughton J, Robinson J, Durgesh V (2003) Oil-film interferometry measurement of skin friction-analysis summary and description of matlab program. In *20th International Congress on Instrumentation in Aerospace Simulation Facilities*, 2003. ICIAF'03., pp 169–178. IEEE
- Naughton JW, Liu T (2007) Photogrammetry in oil-film interferometry. *AIAA J* 45(7):1620–1629
- Naughton JW, Sheplak M (2002) Modern developments in shear-stress measurement. *Prog Aerospace Sci* 38(6–7):515–570
- Naughton JW, Viken S, Greenblatt D (2006) Skin friction measurements on the nasa hump model. *AIAA J* 44(6):1255–1265
- Otsu N (1979) A threshold selection method from gray-level histograms. *IEEE Transact Syst Man Cybern* 9(1):62–66
- Oweis GF, Winkel ES, Cutbrith JM, Ceccio SL, Perlin M, Dowling DR (2010) The mean velocity profile of a smooth-flat-plate turbulent boundary layer at high Reynolds number. *J Fluid Mech* 665:357–381
- Rezaeiravesh S, Vinuesa R, Liefvendahl M, Schlatter P (2018) Assessment of uncertainties in hot-wire anemometry and oil-film interferometry measurements for wall-bounded turbulent flows. *Eur J Mech-B/Fluids* 72:57–73
- Ruedi J, Nagib H, Österlund J, Monkewitz P (2003) Evaluation of three techniques for wall-shear measurements in three-dimensional flows. *Exp Fluids* 35(5):389–396
- Segalini A, Rüedi JD, Monkewitz PA (2015) Systematic errors of skin-friction measurements by oil-film interferometry. *J Fluid Mech* 773:298–326
- Simmons D, Thomas FO, Corke TC (2019) Evidence of surface curvature effects in smooth body flow separation experiments. In *AIAA Aviation 2019 Forum*, pp 2849
- Simmons D, Thomas FO, Corke TC, Hussain F (2022) Experimental characterization of smooth body flow separation topography and topology on a two-dimensional geometry of finite span. *J Fluid Mech* 944:A42
- Simmons DJ (2020) An Experimental Investigation of Smooth-Body Flow Separation. Ph.D. thesis, University Of Notre Dame
- Squire LC (1961) The motion of a thin oil sheet under the steady boundary layer on a body. *J Fluid Mech* 11(2):161–179
- Tanner L, Blows L (1976) A study of the motion of oil films on surfaces in air flow, with application to the measurement of skin friction. *J Phys E: Sci Instrum* 9(3):194
- Uzun A, Malik MR (2021) High-fidelity simulation of turbulent flow past gaussian bump. *AIAA J* 1–20
- Uzun A, Malik MR (2021) Simulation of a turbulent flow subjected to favorable and adverse pressure gradients. *Theoretical Comput Fluid Dynamics* 35(3):293–329
- Von Karman T (1934) Turbulence and skin friction. *J Aeronaut Sci* 1(1):1–20
- Wadcock AJ, Yamauchi GK, Driver DM (1999) Skin friction measurements on a hovering full-scale tilt rotor. *J Am Helicopter Soc* 44(4):312–319
- Williams O, Samuell M, Sarwas ES, Robbins M, Ferrante A (2020) Experimental study of a CFD validation test case for turbulent separated flows. In *AIAA Scitech 2020 Forum*, pp 0092
- Womack KM, Meneveau C, Schultz MP (2019) Comprehensive shear stress analysis of turbulent boundary layer profiles. *J Fluid Mech* 879:360–389
- Zhang Z (2000) A flexible new technique for camera calibration. *IEEE Transact Pattern Anal Mach Intell* 22(11):1330–1334
- Ziliac GC (1996) Further developments of the fringe-imaging skin friction technique. Technical report, NASA Tech Memorandum, p 110425

Publisher's Note Springer Nature remains neutral with regard to jurisdictional claims in published maps and institutional affiliations.